Published in final edited form as:

J Magn Reson Imaging. 2010 June ; 31(6): 1371–1378. doi:10.1002/jmri.22179.

Pharmacokinetic Mapping for Lesion Classification in Dynamic Breast MRI

Matthias C. Schabel, PhD[1,2,*], **Glen R. Morrell, MD PhD**[1,2], **Karen Y. Oh, MD**[3], **Cheryl A. Walczak, MD**[1], **R. Brad Barlow, BS**[4], and **Leigh A. Neumayer, MD MS**[5]

[1]University of Utah Department of Radiology 30 N 1900 E Salt Lake City, UT 84132

[2]Utah Center for Advanced Imaging Research 729 Arapeen Drive Salt Lake City, UT 84108-1218

[3]Department of Radiology Oregon Health & Science University 3181 SW Sam Jackson Park Road, Mail Code L340 Portland, OR 97239

[4]University of Utah School of Medicine 30 N 1900 E Salt Lake City, UT 84132

[5]University of Utah Department of Surgery School of Medicine 30 N 1900 E Salt Lake City, UT 84132

Abstract

PURPOSE—To prospectively investigate whether a rapid dynamic MRI protocol, in conjunction with pharmacokinetic modeling, could provide diagnostically useful information for discriminating biopsy-proven benign lesions from malignancies.

MATERIALS AND METHODS—Patients referred to breast biopsy based on suspicious screening findings were eligible. After anatomic imaging, patients were scanned using a dynamic protocol with complete bilateral breast coverage. Maps of pharmacokinetic parameters representing transfer constant (K^{trans}), efflux rate constant (k_{ep}), blood plasma volume fraction (v_p), and extracellular extravascular volume fraction (v_e) were averaged over lesions and used, with biopsy results, to generate receiver operating characteristic curves for linear classifiers using one, two, or three parameters.

RESULTS—Biopsy and imaging results were obtained from 93 lesions in 74 of 78 study patients. Classification based on K^{trans} and k_{ep} gave the greatest accuracy, with an area under the ROC curve of 0.915, sensitivity of 91%, and specificity of 85%, compared to values of 88% and 68%, respectively, obtained in a recent study of clinical breast MRI in a similar patient population.

CONCLUSION—Pharmacokinetic classification of breast lesions is practical on modern MRI hardware and provides significant accuracy for identification of malignancies. Sensitivity of a two-parameter linear classifier is comparable to that reported in a recent multi-center study of clinical breast MRI, while specificity is significantly higher.

Keywords

dynamic contrast-enhanced MRI; breast imaging; Tofts model

* Corresponding author : 801-587-9413 (tel) 801-585-3592 (fax) matthias.schabel@hsc.utah.edu.

INTRODUCTION

Breast MRI interpretation involves the evaluation of both morphologic features and qualitative enhancement kinetics of lesions (1-3). Unfortunately, optimization of spatial resolution (for lesion morphology) and temporal resolution (for contrast kinetics) both decrease signal, so a compromise must be struck balancing the two. Recent work looking at the impact of improving spatial resolution demonstrated that an imaging protocol with 0.6 × 0.8 mm in-plane resolution and 116 second temporal resolution resulted in significantly superior diagnostic accuracy relative to the use of a protocol with 1.25 × 1.25 mm in-plane resolution and 69 second temporal resolution (4). Because the sampling time needed for characterization of contrast kinetics is significantly shorter than this (5,6), neither of these sequences was sufficiently rapid to accurately estimate pharmacokinetic parameters and no attempt was made to do so, and it remains an open question what benefit, if any, is provided by acquisition of high temporal resolution breast MRI data.

The purpose of this study was to prospectively investigate whether use of an imaging protocol with substantially higher temporal resolution than is typical for clinical breast dynamic contrast-enhanced (DCE) MRI, in conjunction with quantitative pharmacokinetic modeling, could provide diagnostically useful information for discriminating biopsy-proven benign lesions from malignancies.

MATERIALS AND METHODS

Study Design and Inclusion Criteria

We performed a prospective study in 78 patients referred to breast biopsy based on suspicious mammogram, ultrasound, and/or clinical breast exam. Participants were eligible for inclusion in the study if they were female and at least 18 years of age, had been referred to breast biopsy independent of any MRI findings, and had no contraindications to MRI scanning or Gd-based contrast agent administration. Consecutive patients meeting the enrollment criteria were given the opportunity to enroll in the study, and all lesions that were scheduled for biopsy (including multiple lesions, either ipsilateral or contralateral, in individual patients) were included. Prior to the biopsy procedure, patients underwent a modified bilateral breast MRI protocol, described in detail below. After biopsy, imaging findings corresponding to the biopsy site were correlated with pathology. The resulting pharmacokinetic parameters and biopsy results were used to generate receiver operating characteristic (ROC) curves for linear classifiers using only the contrast kinetic data. Area under the ROC curve (AUC) was used as a statistical figure-of-merit for evaluating classifier performance. The study design was approved by our institutional review board, and patients gave informed written consent after the design and purpose of the study had been explained to them.

Validation of Diagnoses

The final pathologic diagnosis was made following standard procedures for our institution. All pathologists were blinded to study participation status and DCE-MRI results. Tissue specimens were obtained from stereotactic or ultrasound-guided core needle biopsies, wire-

localized excisional biopsy, or mastectomy. Pathologic diagnosis used specimens obtained from the initial core biopsy except when the patient subsequently underwent mastectomy in which case the mastectomy specimens provided the definitive diagnosis.

MR Imaging Protocol

A consistent MRI protocol was followed for all patient scans, performed on a 1.5-T Siemens Avanto scanner with a 7-channel bilateral breast coil (In Vivo Corp.). The protocol consisted of standard T1-weighted axial and sagittal T1- and fat-saturated T2-weighted scans that were identical to the non-contrast portion of the standard clinical breast imaging protocol at our institution. Dynamic imaging was then performed with 9.2-19.7 second time resolution per frame using a fast 3D spoiled gradient echo (SPGR) sequence ($T_R/T_E/\alpha$ = 2.54 ms/1.09 ms/10 degrees, 256 × 104 matrix in the coronal plane giving 1.5mm isotropic resolution). Sufficient slices (between 60 and 128) were obtained to achieve coverage of the breast from nipple to chest wall. Partial (6/8) Fourier encoding was used in both the phase and slice encoding directions to decrease image acquisition time. Five to ten pre-contrast baseline scans were acquired, followed by injection of 20ml of gadodiamide contrast agent (Omniscan (gadodiamide), Amersham Health) through an 18ga IV inserted into the antecubital vein. Contrast injection, using a power injector (MedRad Spectra-Solaris), was performed at a constant rate of 4 ml/s, followed by a flush of 20 ml of saline injected at 2 ml/s. Dynamic data was acquired for a total of 8-10 minutes.

Pharmacokinetic Modeling

The initial step in determination of pharmacokinetic (PK) parameters was conversion of measured signal into contrast concentration vs. time curves. This was accomplished by numerical solution of the theoretical relative signal enhancement, (S-S0)/S0, for an SPGR pulse sequence, as described in Section 2 of Schabel, et al. (7). Both longitudinal and transverse relaxation rates were assumed to vary linearly with concentration and contrast relaxivities were taken from literature values (8). The pre-contrast longitudinal relaxation time, $T_{1,0}$, was set to a value of 820 ms appropriate for breast parenchyma (9). An extended Kety model (10,11) incorporating parameters for the transfer constant representing permeability-surface area product (K^{trans}), the contrast efflux rate constant (k_{ep}), and fractional blood plasma volume fraction (v_p): $C_t(t) = K^{trans} C_p(t) \otimes e^{-k_{ep}t} + v_p C_p(t)$, was fit to the resulting concentration-time curves, $C_t(t)$, for each voxel. Extracellular extravascular volume fraction was computed as $v_e = K^{trans}/k_{ep}$. The absence of major arteries in the breast makes it difficult to measure the arterial input function (AIF) without significantly increasing acquisition time, so a population-averaged AIF was used to model the time-dependent contrast concentration in the blood plasma, $C_p(t)$. This model AIF, derived from studies in other tumor patients performed at our institution with an identical injection protocol to the one used for this study, is similar to a recently published empirical AIF (12). Peak blood plasma concentration was normalized to total contrast dose per kg of body mass and computed using an assumed hematocrit value of 0.45. Bolus arrival time was allowed to vary between 0 and 30 seconds, giving an independently estimated fourth parameter accounting for the time delay between bolus injection and its arrival in the breast. Data from each non-noise voxel (voxels for which the mean pre-contrast signal was at least three

standard deviations above the mean signal in a manually-identified extracorporeal ROI) in the imaging volume was fit independently, resulting in 3D maps of the pharmacokinetic parameters covering the full volume of both breasts. The regression covariance matrix, computed using concentration measurement uncertainties derived from analysis of the SPGR signal equation, was used to generate corresponding maps of uncertainty in estimated pharmacokinetic parameter values (7).

Determination of Regions of Interest

Significance masks were generated for each parameter by selecting voxels for which the measured parameter values exceeded the measurement uncertainty, determined as described above. For K^{trans} and v_p, fitting of voxels dominated by noise results in values that trend toward zero, so masking of these parameters is not critical. In contrast, k_{ep} estimates can become spuriously large for noisy data. For this reason, the k_{ep} significance mask was used to define lesion regions of interest (ROI). To minimize speckle noise in the resulting mask, small clusters less than 8 voxels in volume (27 mm^3) were pruned from the mask using an automated cluster labeling algorithm.

Placement of ROIs on the PK parameter maps was based on lesion location as noted in the initial screening and/or biopsy reports. ROIs were generated from the k_{ep} significance mask using a 3D region-growing algorithm with the starting seed placed manually. Because contrast enhancement kinetics in blood vessels can mimic that in tumors, blood vessels identified in the pre-contrast anatomic images were manually pruned from the resulting ROIs. Median value and interquartile range for the four PK parameters were computed by averaging over the entire three-dimensional lesion ROIs. Image processing and statistical data analysis was performed with the OsiriX open source DICOM viewer using custom plugins (www.osirix-viewer.com), MATLAB (The MathWorks Inc.), and Mathematica (Wolfram Research Inc.).

Receiver Operating Characteristic Curves

We generated receiver operating characteristic (ROC) curves for classification using each of the four PK parameters using a standard method (13). We also considered the four unique linear classifiers that can be generated from independent pairs of these parameters: K^{trans} and k_{ep}, K^{trans} and v_p, k_{ep} and v_p, and v_p and v_e, as well as the linear classifier using all three independent PK parameters: K^{trans}, k_{ep}, and v_p. Combinations of K^{trans} and k_{ep} with v_e were not evaluated because of the dependency implied by the constitutive relationship $v = K^{trans}/k_{ep}$. For any two paired parameters, p_1 and p_2, ROCs were computed by applying the method referenced above to the linear combination $p = p_1\cos\theta - p_2\sin\theta$ for θ varying from -180 degrees to 180 degrees in one degree increments. For each θ, the area under the ROC curve was computed by trapezoid rule integration. The best possible linear classifier was then determined by maximizing the AUC as a function of θ. A similar algorithm was implemented using two angles for the three parameter case: K^{trans}, k_{ep}, and v_p.

RESULTS

Seventy eight patients met enrollment criteria and gave informed consent to participate in this study. The mean age of the participants was 45.3 years (range: 26-68). Biopsy results were obtained in 93 lesions from 74 of these patients. Diagnoses were made on the basis of histologic examination of tissue specimens from stereotactic core biopsy (N = 13), ultrasound-guided core biopsy (N = 42), MR guided core biopsy (N = 4), excisional biopsy (N = 10), or mastectomy (N = 24) by pathologists experienced in breast cancer diagnosis.

Pathology

Sixty of the 93 biopsied lesions were diagnosed as benign including 37 instances of fibrocystic change, adenosis, inflammation, etc...(in 29 patients), 5 papillomas (in 5 patients), and 18 fibroadenomas (in 16 patients). Thirty-three lesions were diagnosed as atypical or malignant, including 1 atypical apocrine metaplasia, 1 atypical papilloma, 2 atypical ductal hyperplasias (in 2 patients), 1 lobular carcinoma *in situ* (LCIS), 5 ductal carcinomas *in situ* (in 4 patients), 1 invasive lobular carcinoma, and 22 invasive ductal carcinomas (in 14 patients).

MR Imaging

DCE-MRI data of acceptable quality was obtained in 74 of the 78 patients enrolled. Of the four whose data was rejected, one was eliminated due to an incorrect imaging protocol, one due to excessive patient motion, one due to claustrophobia, and one due to scanner hardware failure. Pre-contrast signal-to-noise ratio (SNR) for the dynamic scans was generally between 10 and 15 in lesions. In the majority of biopsied lesions (61/93) an ROI corresponding to enhancement in the biopsied region of the breast could be identified. In the remaining 32 lesions, nothing was identifiable on the significance mask and PK parameter values were set to zero. All lesions that proved to be atypical or malignant were prospectively identifiable in the PK maps. Data from seven patients required additional manual pruning of the region-growing ROI to isolate the identified lesion, typically as the result of elevated contrast enhancement in the uninvolved breast parenchyma. In these cases, a threshold K^{trans} value of 0.04/min was used to define lesion ROI boundaries. Chi-squared values for the pharmacokinetic model regressions were essentially indistinguishable between normal breast parenchymal tissues, benign lesions, and malignancies, indicating that the model fits were comparably good across all tissues investigated.

Lesion-averaged concentration-time curves are shown in Figure 1 for normal breast parenchyma (no observed pathologic changes on biopsy, corresponding to Patient A in Figure 2), fibroadenoma (corresponding to Patient C in Figure 2), and invasive ductal carcinoma (corresponding to Patient F in Figure 2). Curves in this figure were time-shifted so that the bolus arrival times were synchronized between patients. Figure 2 shows T1-weighted (first row) and fat-saturated T2-weighted (second row) anatomic images acquired in the sagittal plane in six patients, labeled A-F, along with spatially co-registered, sagitally reformatted maps of the K^{trans} (third row) and k_{ep} parameters (fourth row). Patient A was diagnosed with benign fibrocystic disease, and patients B and C with benign fibroadenomas. Patient D was found to have a small focus of ductal carcinoma *in situ* near the chest wall,

while patients E and F both were diagnosed with invasive ductal carcinoma. Maps of k_{ep} were masked as described above, but the masks used for displayed images were not manually pruned. Artifacts in k_{ep} arising from chest wall motion and lung tissue in the field of view are visible in the data on patients C and D, and blood vessels adjacent to the tumor are visible as small foci in the data from patient F.

Data Analysis

Median value and interquartile range computed for lesion-averaged pharmacokinetic parameters are given in Table 1. The upper portion shows results for biopsy-proven benign lesions, separated into five categories: lesions with no visible abnormality, visible lesions, papillomas, fibroadenomas, and other. The lower portion of the table shows results for atypical lesions (including atypical papilloma, atypical apocrine metaplasia, atypical ductal hyperplasia, and LCIS), and malignant lesions (including DCIS, ILC, and IDC), both aggregated and separately. Atypical lesions were grouped with malignant lesions because these lesions are often associated with elevated risk for cancer (relative risk of 3.9-13 (14-16)). In the case of atypical hyperplasia, many (14-31% (17-20)) are found to be malignant on excisional biopsy, and it is conventional to perform excisional biopsy of proliferative lesions with atypica including ductal or lobular hyperplasias and LCIS.

An unequal variance t-test was applied to the lesion-averaged values of the four PK parameters given in Table 1 to test the null hypothesis that the mean values differ between benign and atypical/malignant lesions. Non-visualized lesions (all of which proved to be benign) were included with parameter values of K^{trans}, k_{ep}, and v_p equal to zero. For comparison between all benign lesions and atypical/malignant lesions, the difference in means was found to be significant at the 99.9% level ($p \leq 0.001$) for all four PK parameters ($p|K^{trans} = 1.2 \times 10^{-8}$, $p|k_{ep} = 7.0 \times 10^{-18}$, $p|v_p = 1.0 \times 10^{-8}$, $p|v_e = 4.0 \times 10^{-5}$), but not for lesion volume ($p|V = 0.008$). When non-visualized benign lesions are excluded from this comparison, the difference in means remains significant at the 99.9% level only for K^{trans}($p|K^{trans} = 2.6 \times 10^{-4}$), and k_{ep}($p|k_{ep} = 2.0$—10^{-4}), with $p|v_p = 0.09$, $p|v_e = 0.33$, and $p|V = 0.06$.

ROC curves are plotted in Figure 3 for the four individual PK parameters, with k_{ep} indicated by the red line, K^{trans} by the blue line, v_e by the pink line, and v_p by the green line. Overall accuracy, measured by AUC, was highest for k_{ep} (0.894, 95% CI : 0.885-0.903), followed by K^{trans} (0.878, 95% CI : 0.869-0.888), v_e (0.809, 95% CI : 0.798-0.820), and v_p (0.796, 95% CI : 0.776-0.815). ROC curves for the four independent pairs of PK parameters (K^{trans} and k_{ep}, K^{trans} and v_p, k_{ep} and v_p, v_p and v_e) were also computed. Of these four pairs, only the combination of K^{trans} and k_{ep}, shown by the black ROC curve in Figure 3, gave significant improvement in AUC relative to use of k_{ep} alone (0.915 (95% CI : 0.906-0.923) vs 0.894). None of the other three pairs performed significantly better than the ROC using k_{ep} alone (0.881 for K^{trans} and v_p (95% CI : 0.872-0.892), 0.904 for k_{ep} and v_p (95% CI : 0.895-0.914), and 0.810 for v_p and v_e (95% CI : 0.799-0.822)). The three parameter classifier using K^{trans}, k_{ep}, and v_p also failed to perform significantly better than the combination of K^{trans} and k_{ep}, giving an identical AUC value of 0.915 (95% CI : 0.906-0.924). The linear classifier maximizing the area under the ROC for K^{trans} and k_{ep} is given by $1.55K^{trans}+0.63k_{ep}$ (slope = -2.46). Figure 4 shows a scatter plot of (K^{trans},k_{ep})

pairs categorized by lesion type. The classifier corresponding to a sensitivity of 91% and a specificity of 85%, $k_{ep} \geq 0.373 - 2.46K^{trans}$, is indicated by the dashed gray line. It is also important to note that, because the lesions with atypia observed in our study all lie near the optimal linear classifier line, grouping them with benign lesions has little effect on AUC (for example, for the two-parameter linear classifier using K^{trans} and k_{ep}, the AUC actually increases slightly, to 0.921).

DISCUSSION

The observation that K^{trans}, k_{ep}, and v_p are all elevated in breast tumors is consistent with the results of numerous studies in a range of cancers (21-24). Early studies in breast cancer also found elevated values of K^{trans} and k_{ep} when using a two-compartment model without a direct vascular term (25,26). Our data demonstrate that quantitative pharmacokinetic modeling with adequate spatial and temporal resolution and full bilateral breast coverage is feasible with modern MRI hardware and that these data can be used to discriminate between benign and malignant lesions with high sensitivity and specificity. Linear classifiers using K^{trans}, k_{ep}, v_p, or v_e alone all provide accuracy for lesion characterization, with a 100% negative predictive value (NPV) for lesion-averaged values of K^{trans}<0.04/min or k_{ep}<0.11/min. The combination K^{trans} and k_{ep} provides somewhat increased discriminating power and is quite insensitive to the slope of the classifier line, with the AUC remaining above that of the second best pair of PK parameters (k_{ep} and v_p,) for linear slopes between -0.39 and -8.66. This robustness reflects the fact that both K^{trans} and k_{ep} alone are both relatively good independent classifiers.

Values for the sensitivity and, particularly, specificity of breast MRI reported in the literature vary widely (27), likely a reflection of variations in imaging protocols, institutional expertise, evolving methodologies, and heterogeneous study populations. A recent, large multi-center trial, with eligibility criteria that were essentially identical to ours evaluated the accuracy of conventional breast MRI with radiologist interpretation based on morphology and qualitative assessment of enhancement characteristics. That study reported an overall sensitivity of 88.1% and specificity of 67.7% in 821 patients (28). In comparison, our two-parameter discriminator alone, without interpretation by a radiologist, yields a sensitivity of 91%, a specificity of 85%, a positive predictive value (PPV) of 94%, and a negative predictive value (NPV) of 77%. Future investigations are planned to assess how incorporation of radiologist interpretation of morphology and contrast kinetics impacts overall diagnostic performance when combined with the method reported here.

Parametric modeling of DCE-MRI data in the breast has been performed by a number of other investigators (9,29-31). Our method differs from previously work in that bilateral full-breast coverage is obtained at sufficiently high spatial and temporal resolutions to enable simultaneous morphologic and pharmacokinetic analysis. In addition, our modeling methodology incorporates a vascular term, is performed using bolus contrast injection with variable bolus arrival time and a realistic model input function, and accurately treats both signal nonlinearity with concentration and propagation of errors.

A recent retrospective study investigating the effect of temporal sampling on the performance of breast DCE-MRI in 500 patients using empirical analysis of the concentration-time curves found that decreasing the acquisition time per frame from 60 seconds to 15 seconds led to significant increases in the area under the ROC curve (32). Consistent with our observations, they reported that contrast wash-out was most strongly predictive of malignancy (AUC of 0.85 at 15 second sampling interval), followed by contrast wash-in (AUC of 0.72 at 15 second sampling interval). The former value is comparable to our AUC of 0.894 for k_{ep} alone, while our AUC of 0.878 for K^{trans} alone is notably higher than that for the wash-in AUC, as is our AUC of 0.915 for the linear combination of K^{trans} and k_{ep}. This suggests that pharmacokinetic modeling may provide additional diagnostic accuracy beyond qualitative analysis of curve shape.

Study Limitations

This study had several limitations. First, while the data presented were acquired quite rapidly by the standards of conventional breast MRI, our temporal resolution is still near or above the limit where PK parameters, particularly K^{trans} and v_p, can be accurately estimated (6,33,34). The referenced studies suggest that sampling intervals should be less than 10 seconds for accurate estimation of K^{trans} and k_{ep}, and no longer than 6 seconds for v_p with bolus contrast injection. It is likely that decreasing sampling time without corresponding loss of signal-to-noise ratio would lead to improved accuracy in parameter estimates, although the ramifications of doing so for diagnostic accuracy are unknown. There is an extensive and rapidly growing literature on methods using different k-space undersampling schemes for rapid dynamic imaging which could potentially be adapted to breast imaging to allow further improvements in data acquisition rate. Because the first-pass peak duration is short relative to our current sampling time, the greatest improvement is to be expected in estimation of the blood plasma volume fraction, v_p. Second, potential biases in concentration measurements arising from variation of longitudinal relaxation time from the assumed value for breast parenchyma were also not considered in this study. Similarly, deviation of the true flip angle from its nominal value was neglected. Third, scan timing relative to menstrual cycle was not controlled for, leading to the possibility that the data could have been biased in some patients. It is known that menstrual phase can significantly impact enhancement patterns in the breast (35-37). Because patients were already scheduled for biopsy procedure prior to enrollment in the study, the time interval between MRI and biopsy was fixed (ranging from one hour to several days). Nevertheless, as imaging during the secretory phase of menstruation is generally recognized to degrade the accuracy of breast MRI, the performance of the methods described here would likely be improved by restriction of imaging to the early phase of the menstrual cycle.

Practical Applications

The results presented here demonstrate that pharmacokinetic modeling of contrast enhancement in the breast is feasible with modern, unmodified, MRI scanner hardware and allows discrimination between benign and malignant lesions with high sensitivity and specificity, independent of radiologist interpretation of lesion morphology and/or qualitative contrast kinetics. Unlike conventional interpretation of breast MRI data, the pharmacokinetic modeling approach provides a quantitative algorithm for classifying

suspicious breast lesions. As such, it is potentially amenable to automation (e.g. incorporation into a computer-aided detection system), which could significantly simplify and streamline the currently complex and time-consuming process of reading breast MRIs. In addition, pharmacokinetic modeling appears to have the potential to substantially improve the specificity of breast MRI over current methods of interpretation, and could reduce the false positive rate of clinical breast MRI without sacrificing its sensitivity for detection of lesions occult to other breast imaging modalities.

ACKNOWLEDGEMENTS

This work was supported by the National Institute of Biomedical Imaging and Bioengineering under grant K25 #EB005077, the National Cancer Institute under grant K08 CA112449, and the Ben and Iris Margolis Foundation. M.C.S. would like to acknowledge his research mentors Drs. Dennis Parker, Edward Di Bella, Wallace Akerley, and Saundra Buys for their advice and support.

Grant Support : M.C.S. : NIBIB K25EB005077, Ben B. and Iris M. Margolis Foundation, Benning Foundation G.R.M. : NCI K08CA112449

REFERENCES

1. Kuhl CK, Mielcareck P, Klaschik S, et al. Dynamic breast MR imaging: are signal intensity time course data useful for differential diagnosis of enhancing lesions? Radiology. 1999; 211(1):101–110. [PubMed: 10189459]
2. Nunes LW. Architectural-based interpretations of breast MR imaging. Magn Reson Imaging Clin N Am. 2001; 9(2):303–320. vi. [PubMed: 11493421]
3. Nunes LW, Schnall MD, Orel SG, et al. Breast MR imaging: interpretation model. Radiology. 1997; 202(3):833–841. [PubMed: 9051042]
4. Kuhl CK, Schild HH, Morakkabati N. Dynamic bilateral contrast-enhanced MR imaging of the breast: trade-off between spatial and temporal resolution. Radiology. 2005; 236(3):789–800. [PubMed: 16118161]
5. Aerts HJ, van Riel NA, Backes WH. System identification theory in pharmacokinetic modeling of dynamic contrast-enhanced MRI: Influence of contrast injection. Magnetic resonance in medicine : official journal of the Society of Magnetic Resonance in Medicine / Society of Magnetic Resonance in Medicine. 2008; 59(5):1111–1119.
6. Lopata RG, Backes WH, van den Bosch PP, van Riel NA. On the identifiability of pharmacokinetic parameters in dynamic contrast-enhanced imaging. Magnetic resonance in medicine : official journal of the Society of Magnetic Resonance in Medicine / Society of Magnetic Resonance in Medicine. 2007; 58(2):425–429.
7. Schabel MC, Parker DL. Uncertainty and bias in contrast concentration measurements using spoiled gradient echo pulse sequences. Physics in medicine and biology. 2008; 53(9):2345–2373. [PubMed: 18421121]
8. Rohrer M, Bauer H, Mintorovitch J, Requardt M, Weinmann HJ. Comparison of magnetic properties of MRI contrast media solutions at different magnetic field strengths. Investigative radiology. 2005; 40(11):715–724. [PubMed: 16230904]
9. Brix G, Kiessling F, Lucht R, et al. Microcirculation and microvasculature in breast tumors: pharmacokinetic analysis of dynamic MR image series. Magnetic resonance in medicine : official journal of the Society of Magnetic Resonance in Medicine / Society of Magnetic Resonance in Medicine. 2004; 52(2):420–429.
10. Tofts PS, Brix G, Buckley DL, et al. Estimating kinetic parameters from dynamic contrast-enhanced T(1)-weighted MRI of a diffusable tracer: standardized quantities and symbols. Journal of magnetic resonance imaging : JMRI. 1999; 10(3):223–232. [PubMed: 10508281]
11. Harrer JU, Parker GJ, Haroon HA, et al. Comparative study of methods for determining vascular permeability and blood volume in human gliomas. J Magn Reson Imaging. 2004; 20(5):748–757. [PubMed: 15503330]

12. Parker GJ, Roberts C, Macdonald A, et al. Experimentally-derived functional form for a population-averaged high-temporal-resolution arterial input function for dynamic contrast-enhanced MRI. Magnetic resonance in medicine : official journal of the Society of Magnetic Resonance in Medicine / Society of Magnetic Resonance in Medicine. 2006; 56(5):993–1000.
13. Fawcett T. ROC Graphs: Notes and Practical Considerations for Researchers. HP Labs Techical Report 2003-04. 2003
14. Dupont WD, Page DL. Risk factors for breast cancer in women with proliferative breast disease. N Engl J Med. 1985; 312(3):146–151. [PubMed: 3965932]
15. Dupont WD, Parl FF, Hartmann WH, et al. Breast cancer risk associated with proliferative breast disease and atypical hyperplasia. Cancer. 1993; 71(4):1258–1265. [PubMed: 8435803]
16. Marshall LM, Hunter DJ, Connolly JL, et al. Risk of breast cancer associated with atypical hyperplasia of lobular and ductal types. Cancer Epidemiol Biomarkers Prev. 1997; 6(5):297–301. [PubMed: 9149887]
17. Dmytrasz K, Tartter PI, Mizrachy H, Chinitz L, Rosenbaum Smith, Estabrook A. The significance of atypical lobular hyperplasia at percutaneous breast biopsy. Breast J. 2003; 9(1):10–12. [PubMed: 12558664]
18. Margenthaler JA, Duke D, Monsees BS, Barton PT, Clark C, Dietz JR. Correlation between core biopsy and excisional biopsy in breast high-risk lesions. Am J Surg. 2006; 192(4):534–537. [PubMed: 16978969]
19. Bedei L, Falcini F, Sanna PA, et al. Atypical ductal hyperplasia of the breast: the controversial management of a borderline lesion: experience of 47 cases diagnosed at vacuum-assisted biopsy. Breast. 2006; 15(2):196–202. [PubMed: 16055333]
20. Irfan K, Brem RF. Surgical and mammographic follow-up of papillary lesions and atypical lobular hyperplasia diagnosed with stereotactic vacuum-assisted biopsy. Breast J. 2002; 8(4):230–233. [PubMed: 12100116]
21. Barrett T, Brechbiel M, Bernardo M, Choyke PL. MRI of tumor angiogenesis. Journal of magnetic resonance imaging : JMRI. 2007; 26(2):235–249. [PubMed: 17623889]
22. Hylton N. Dynamic contrast-enhanced magnetic resonance imaging as an imaging biomarker. J Clin Oncol. 2006; 24(20):3293–3298. [PubMed: 16829653]
23. O'Connor JP, Jackson A, Parker GJ, Jayson GC. DCE-MRI biomarkers in the clinical evaluation of antiangiogenic and vascular disrupting agents. Br J Cancer. 2007; 96(2):189–195. [PubMed: 17211479]
24. Huang W, Li X, Morris EA, et al. The magnetic resonance shutter speed discriminates vascular properties of malignant and benign breast tumors in vivo. Proc Natl Acad Sci U S A. 2008; 105(46):17943–17948. [PubMed: 19004780]
25. Mussurakis S, Buckley DL, Drew PJ, et al. Dynamic MR imaging of the breast combined with analysis of contrast agent kinetics in the differentiation of primary breast tumours. Clin Radiol. 1997; 52(7):516–526. [PubMed: 9240704]
26. Hulka CA, Edmister WB, Smith BL, et al. Dynamic echo-planar imaging of the breast: experience in diagnosing breast carcinoma and correlation with tumor angiogenesis. Radiology. 1997; 205(3): 837–842. [PubMed: 9393545]
27. Peters NH, Borel Rinkes IH, Zuithoff NP, Mali WP, Moons KG, Peeters PH. Meta-analysis of MR imaging in the diagnosis of breast lesions. Radiology. 2008; 246(1):116–124. [PubMed: 18024435]
28. Bluemke DA, Gatsonis CA, Chen MH, et al. Magnetic resonance imaging of the breast prior to biopsy. Jama. 2004; 292(22):2735–2742. [PubMed: 15585733]
29. Port RE, Knopp MV, Hoffmann U, Milker-Zabel S, Brix G. Multicompartment analysis of gadolinium chelate kinetics: blood-tissue exchange in mammary tumors as monitored by dynamic MR imaging. Journal of magnetic resonance imaging : JMRI. 1999; 10(3):233–241. [PubMed: 10508282]
30. Radjenovic A, Dall BJ, Ridgway JP, Smith MA. Measurement of pharmacokinetic parameters in histologically graded invasive breast tumours using dynamic contrast-enhanced MRI. Br J Radiol. 2007

31. Vincensini D, Dedieu V, Eliat PA, et al. Magnetic resonance imaging measurements of vascular permeability and extracellular volume fraction of breast tumors by dynamic Gd-DTPA-enhanced relaxometry. Magnetic resonance imaging. 2007; 25(3):293–302. [PubMed: 17371717]

32. El Khouli RH, Macura KJ, Barker PB, Habba MR, Jacobs MA, Bluemke DA. Relationship of temporal resolution to diagnostic performance for dynamic contrast enhanced MRI of the breast. J Magn Reson Imaging. 2009; 30(5):999–1004. [PubMed: 19856413]

33. Di Giovanni P, Azlan CA, Ahearn TS, Semple SI, Gilbert FJ, Redpath TW. The accuracy of pharmacokinetic parameter measurement in DCE-MRI of the breast at 3 T. Phys Med Biol. 2010; 55(1):121–132. [PubMed: 20009182]

34. Henderson E, Rutt BK, Lee TY. Temporal sampling requirements for the tracer kinetics modeling of breast disease. Magn Reson Imaging. 1998; 16(9):1057–1073. [PubMed: 9839990]

35. Delille JP, Slanetz PJ, Yeh ED, Kopans DB, Garrido L. Physiologic changes in breast magnetic resonance imaging during the menstrual cycle: perfusion imaging, signal enhancement, and influence of the T1 relaxation time of breast tissue. The breast journal. 2005; 11(4):236–241. [PubMed: 15982388]

36. Kuhl CK, Bieling HB, Gieseke J, et al. Healthy premenopausal breast parenchyma in dynamic contrast-enhanced MR imaging of the breast: normal contrast medium enhancement and cyclical-phase dependency. Radiology. 1997; 203(1):137–144. [PubMed: 9122382]

37. Müller-Schimpfle M, Ohmenhaüser K, Stoll P, Dietz K, Claussen CD. Menstrual cycle and age: influence on parenchymal contrast medium enhancement in MR imaging of the breast. Radiology. 1997; 203(1):145–149. [PubMed: 9122383]

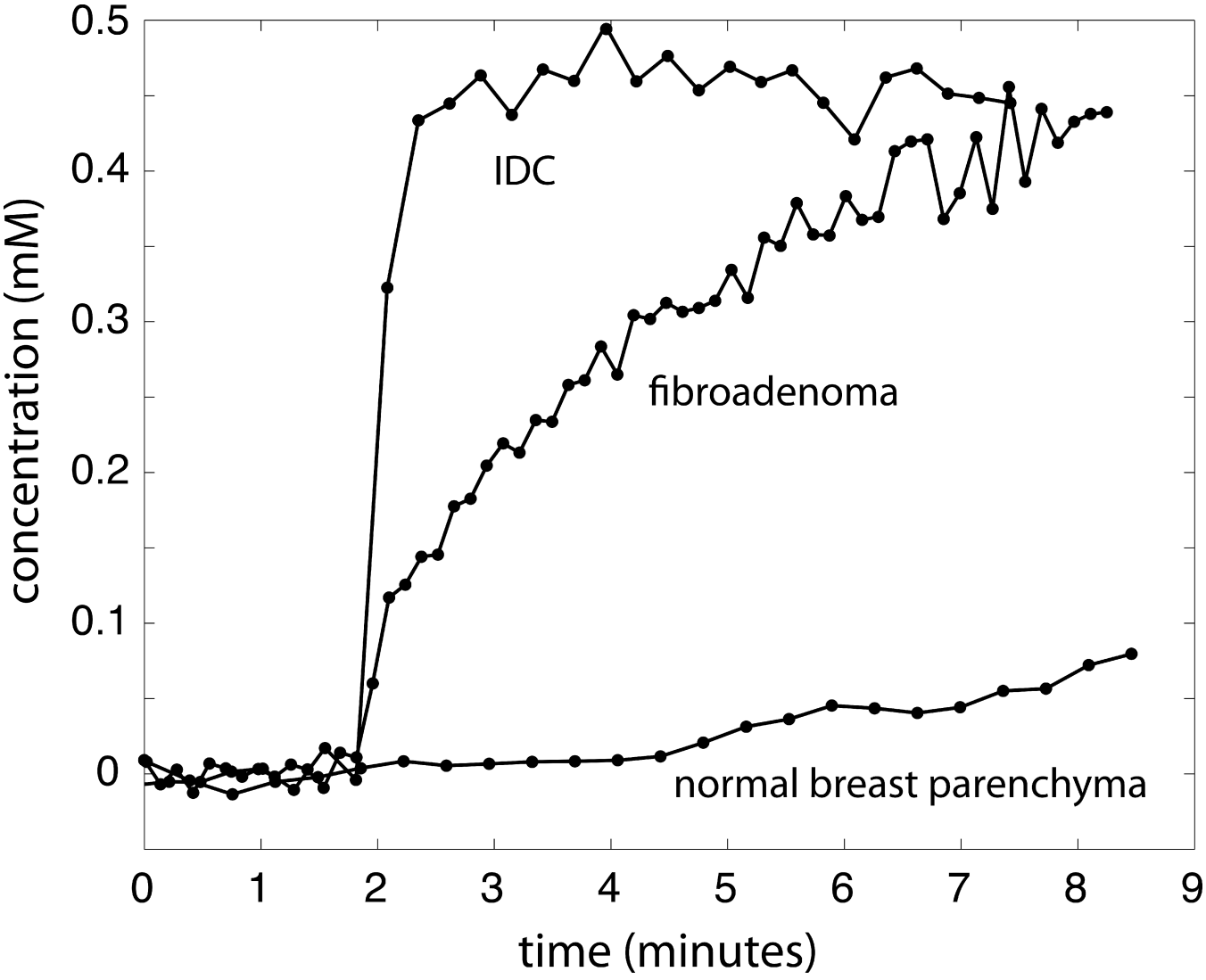

Figure 1.

Lesion-averaged concentration-time curves are plotted for three study patients, one with no pathologic changes (normal breast parenchyma, corresponding to Patient A in Figure 2), one with biopsy-proven fibroadenoma (corresponding to Patient C in Figure 2), and one with biopsy-proven invasive ductal carcinoma (corresponding to Patient F in Figure 2).

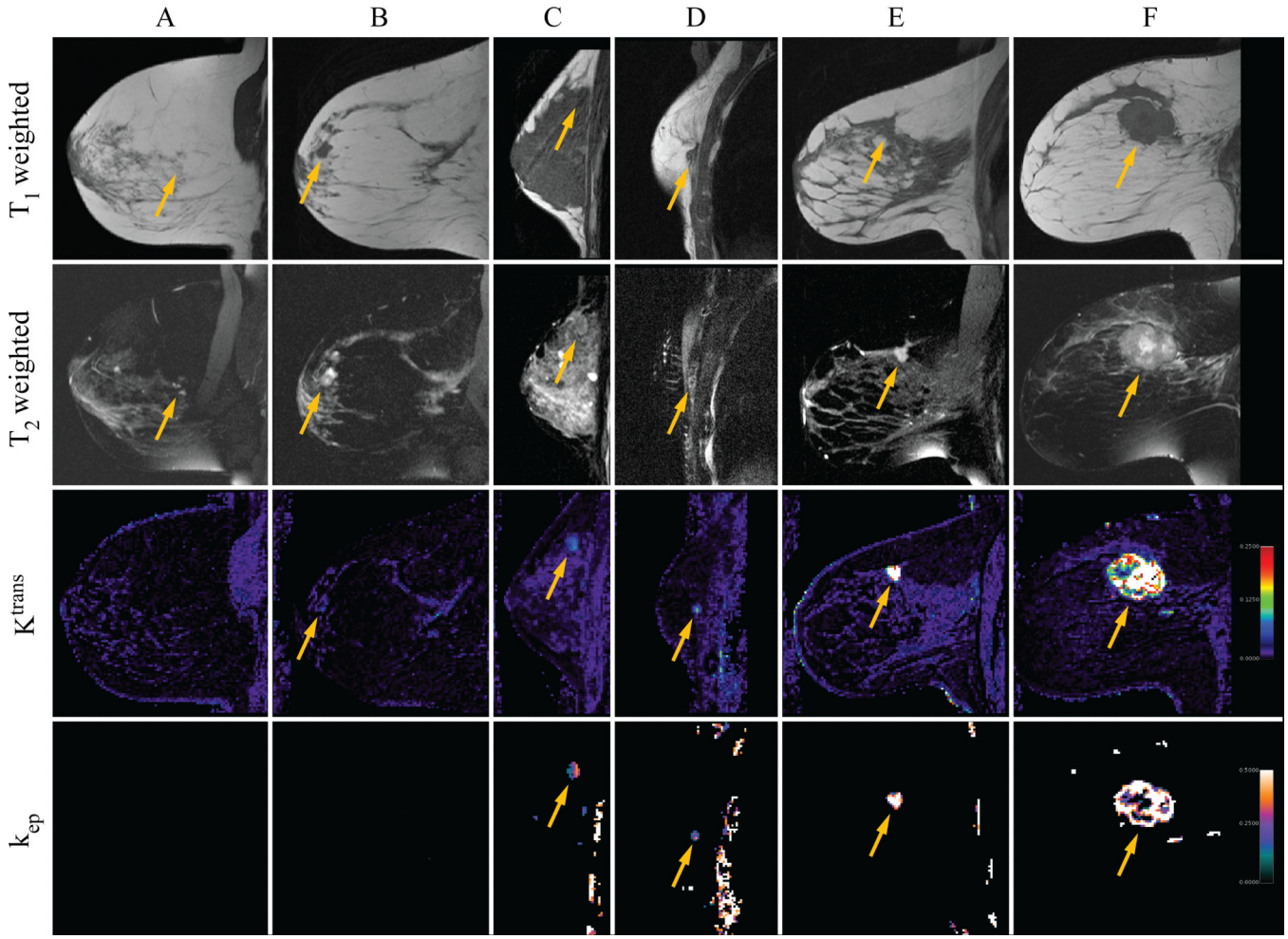

Figure 2.

T1 and fat-saturated T2-weighted anatomic images are shown for six study patients (A-F), along with the corresponding sagittally-reformatted maps of K^{trans} (in 1/min) and k_{ep} (in 1/min). T1-weighted images are plotted in the first row, fat-saturated T2-weighted images in the second, K^{trans} in the third, and k_{ep} in the fourth. The approximate location of the biopsied lesion is indicated by arrows in each panel. Patient A was diagnosed with mammary fibrosis, patients B and C with benign fibroadenoma, patient D with ductal carcinoma *in situ*, and patients E and F with invasive ductal carcinoma. Maps of k_{ep} have been masked as described in the text, but have not been manually edited.

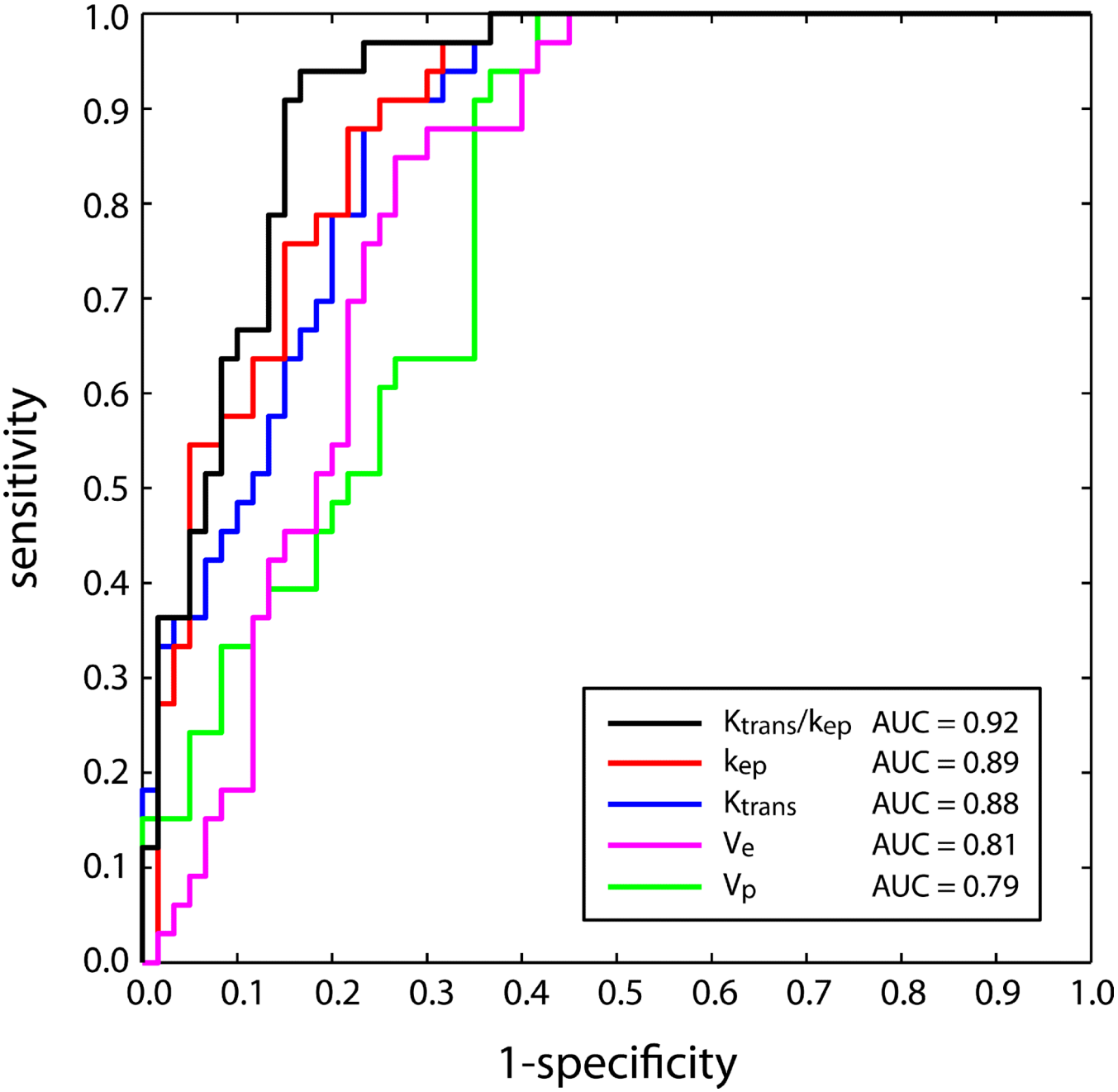

Figure 3.

ROC curves for classification of malignant lesions by k_{ep} (red), K^{trans} (blue), v_e (pink), and v_p (green) individually, and for the linear combination, $1.55K^{trans} + 0.63k_{ep}$, that provides the maximum area under the ROC (black).

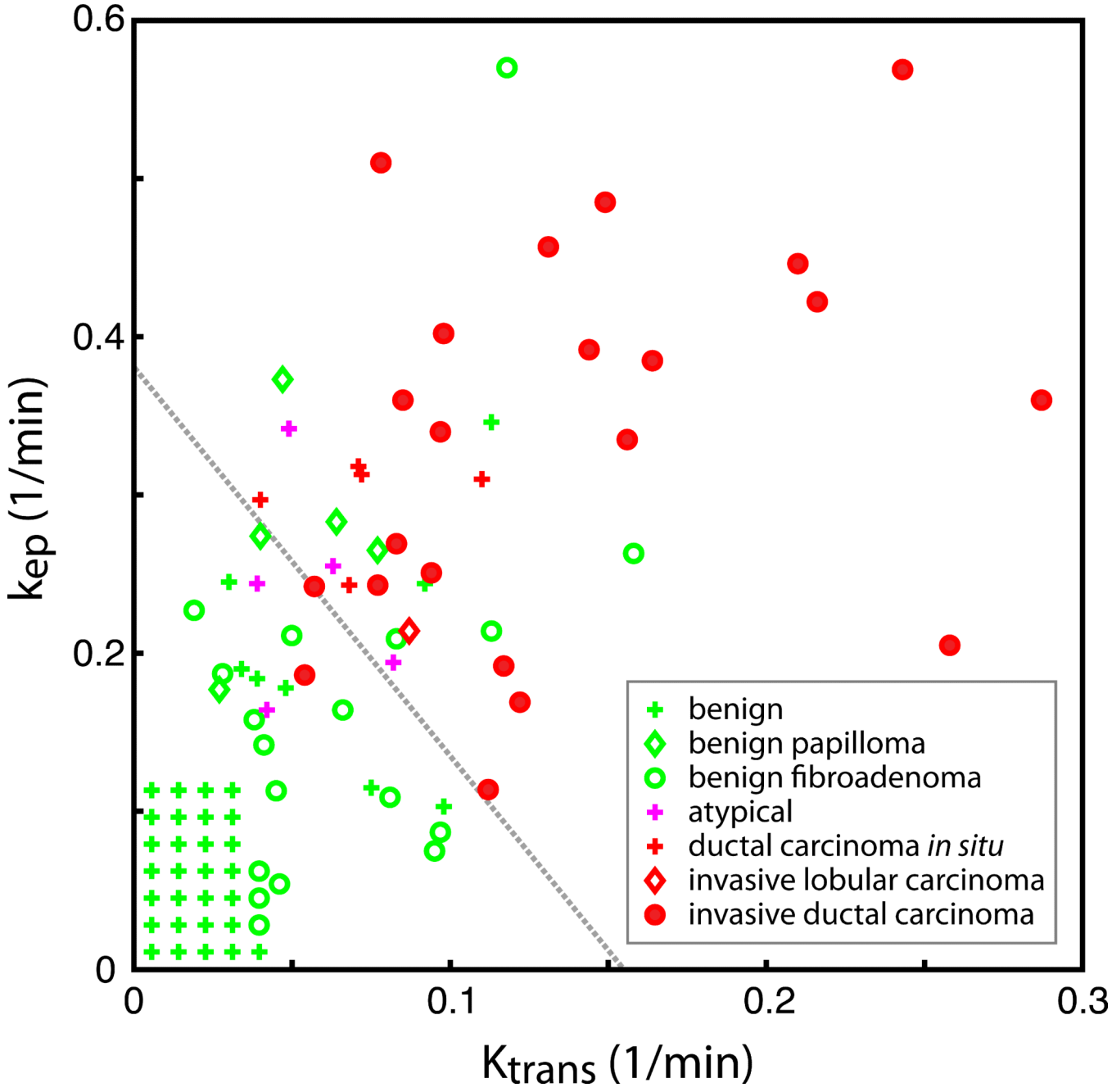

Figure 4.

Scatter plot of k_{ep} vs. K^{trans} for all 93 biopsied lesions from our 74 study patients. Benign lesions are indicated by green symbols (papillomas by green diamonds, fibroadenomas by green circles, and other benign findings by green crosses). The 32 benign lesions that did not reach significance in k_{ep} are shown clustered in the grid at the lower left. Lesions showing atypia are indicated by the pink crosses, ductal carcinoma *in situ* by red crosses, invasive lobular carcinoma by red diamonds, and invasive ductal carcinoma by red circles. The linear

classifier $1.55K^{trans} + 0.63k_{ep} \geq 0.235$, providing 91% sensitivity and 85% specificity for lesion classification (94% PPV, 77% NPV), is shown by the dashed gray line

Table 1

Median values of lesion volume and lesion-averaged pharmacokinetic parameters, with interquartile ranges given parenthetically.

	N	Volume (cc)	K^{trans} (1/min)	k_{ep} (1/min)	v_p (%)	v_e (%)
benign	60	0.00 (0.00-0.22)	0.00 (0.00-0.04)	0.00 (0.00-0.16)	0.0 (0.0-0.4)%	0 (0-21)%
no abnormality visualized	32*	n/a	n/a	n/a	n/a	n/a
visible benign lesions	28	0.40 (0.22-0.57)	0.06 (0.05-0.08)	0.19 (0.16-0.23)	0.5 (0.4-0.8)%	28 (22-39)%
papilloma	5	0.10 (0.08-0.39)	0.05 (0.04-0.06)	0.27 (0.27-0.28)	0.5 (0.4-0.5)%	18 (17-21)%
fibroadenoma	18	0.48 (0.22-0.57)	0.07 (0.05-0.10)	0.16 (0.11-0.21)	0.4 (0.2-0.9)%	28 (24-56)%
other	5	1.43 (0.37-1.89)	0.08 (0.04-0.09)	0.19 (0.18-0.24)	0.9 (0.7-1.4)%	35 (28-41)%
atypical/malignant lesions	33	0.50 (0.19-2.84)	0.09 (0.08-0.12)	0.31 (0.24-0.36)	0.6 (0.4-1.0)%	34 (28-43)%
atypical	5	0.36 (0.09-1.89)	0.05 (0.04-0.06)	0.24 (0.19-0.26)	0.5 (0.4-0.6)%	25 (15-28)%
malignant	28	0.88 (0.33-2.84)	0.11 (0.08-0.13)	0.32 (0.25-0.36)	0.8 (0.4-1.0)%	39 (30-43)%

* In 32 patients no abnormality could be identified on the k_{ep} map. All of these showed benign pathology.